

## Theoretical determination of the Raman spectra of single-crystal forsterite ( $\text{Mg}_2\text{SiO}_4$ )

DAVID A. MCKEOWN,<sup>1,\*</sup> MICHAEL I. BELL,<sup>1</sup> AND RAZVAN CARACAS<sup>2</sup>

<sup>1</sup>Vitreous State Laboratory, The Catholic University of America, 620 Michigan Avenue, N.E., Washington, D.C. 20064, U.S.A.

<sup>2</sup>CNRS, Laboratoire de Sciences de la Terre, Ecole Normale Supérieure de Lyon, Université de Lyon, 46, allée d'Italie, 69364 Lyon, France

### ABSTRACT

Density functional perturbation theory is used to calculate the Raman spectrum of forsterite ( $\text{Mg}_2\text{SiO}_4$ ). In addition to the fundamental mode frequencies and atomic displacements, the scattering intensities are computed from first principles for the first time. Six independent single-crystal Raman spectra are measured for synthetic forsterite, and good agreement is found between calculation and experiment over a range of nearly six orders of magnitude of scattered intensity. Calculated atomic displacements of these fundamental Raman modes generally agree closely with the results of previous lattice dynamics studies. Modes with frequencies above  $500\text{ cm}^{-1}$  consist primarily of motions internal to the  $\text{SiO}_4$  tetrahedra, while those below  $500\text{ cm}^{-1}$  are dominated by Mg2 displacements mixed with  $\text{SiO}_4$  translations and rotations. The considerably larger Raman amplitudes for modes above  $500\text{ cm}^{-1}$  appear to be due to displacements within the highly polarizable oxygen environments surrounded by covalently bonded  $\text{Si}^{4+}$  and ionically bonded  $\text{Mg}^{2+}$ . With regard to calculated frequencies, the theory underestimates frequencies by as much as  $8\text{ cm}^{-1}$  for modes over  $500\text{ cm}^{-1}$ , while it generally overestimates frequencies by as much as  $17\text{ cm}^{-1}$  for modes below  $500\text{ cm}^{-1}$ . An equivalent set of Raman spectra were measured for the Fe end-member of the olivine solid-solution series, fayalite ( $\text{Fe}_2\text{SiO}_4$ ), and compared to the results for forsterite.

**Keywords:** Raman spectroscopy, fayalite, forsterite, density functional theory

### INTRODUCTION

Olivine,  $(\text{Mg,Fe})_2\text{SiO}_4$ , is one of the major mineral constituents of the Earth's crust and upper mantle. It is widespread in various magmatic and metamorphic basic and ultrabasic rocks. Due to its mineralogical importance and its relatively simple structure (Boström 1987) for a silicate (Fig. 1), many of its physical properties have been characterized under various thermodynamic conditions. The study of its spectroscopic properties has been a center of interest for several experimental and computational mineral physicists and petrologists (Noel et al. 2006; Lam et al. 1990; Kolesov and Geiger 2004; Chopelas 1991; Mouri et al. 2008; Iishi 1978). Despite this extensive effort, there remains room for improvement, particularly with regard to the detailed description of the Raman scattering spectrum.

Here, we perform first-principles calculations based on the density functional theory (DFT) (Kohn and Sham 1965) and density functional perturbation theory (DFPT) (Gonze et al. 2005a; Baroni et al. 2001) in the ABINIT implementation (Gonze et al. 2002, 2005b) on the Mg end-member ( $\text{Mg}_2\text{SiO}_4$ , forsterite), computing for the first time the Raman spectrum with both peak positions and intensities. Until recently, calculations of the Raman spectrum of forsterite reported only the peak positions. Now we are able to compute the intensities as well, obtaining the Raman scattering factors from linear response within the DFPT approximation. These were compared with Raman scattering measurements performed on a forsterite synthetic single crystal

in six scattering geometries, corresponding to the independent components of the Raman tensor. This study is part of an ongoing series attempting to calculate the Raman spectra of crystalline silicates of various degrees of structural complexity.

The results presented here for forsterite can be compared with findings from four studies (Noel et al. 2006; Kolesov and Geiger 2004; Chopelas 1991; Iishi 1978) that used various combinations of observation and theory to assign vibrational modes to spectral features. Iishi (1978) used three different models to calculate Raman-mode frequencies and associated eigenmodes. Chopelas (1991) observed changes in Raman features correlated with composition differences among six different olivine samples. Kolesov and Geiger (2004) used Mg isotope substitution and Raman mode frequency shifts observed in the powder Raman spectra of forsterite to determine vibrational assignments for 25 modes. More recently, Noel et al. (2006) used the ab initio program CRYSTAL to calculate frequencies and atomic displacements, as well as Mg, Si, and oxygen isotopic effects on the Raman and IR spectra.

Noel et al. (2006) were able to calculate the frequencies of the zone-center phonons, including the effects of isotopic substitutions. When the Mg2 isotope is changed, modes with frequencies below  $600\text{ cm}^{-1}$  generally shift significantly, with maximum shifts taking place for modes near 200 to  $400\text{ cm}^{-1}$ . When the Si isotope is changed, modes above  $600\text{ cm}^{-1}$  are the most affected, with maximum shifts occurring for modes at the highest frequencies, near  $1000\text{ cm}^{-1}$ . When the oxygen isotope is changed, modes above  $300\text{ cm}^{-1}$  exhibit the greatest effects, with shifts becoming

\* E-mail: davidm@vsl.cua.edu

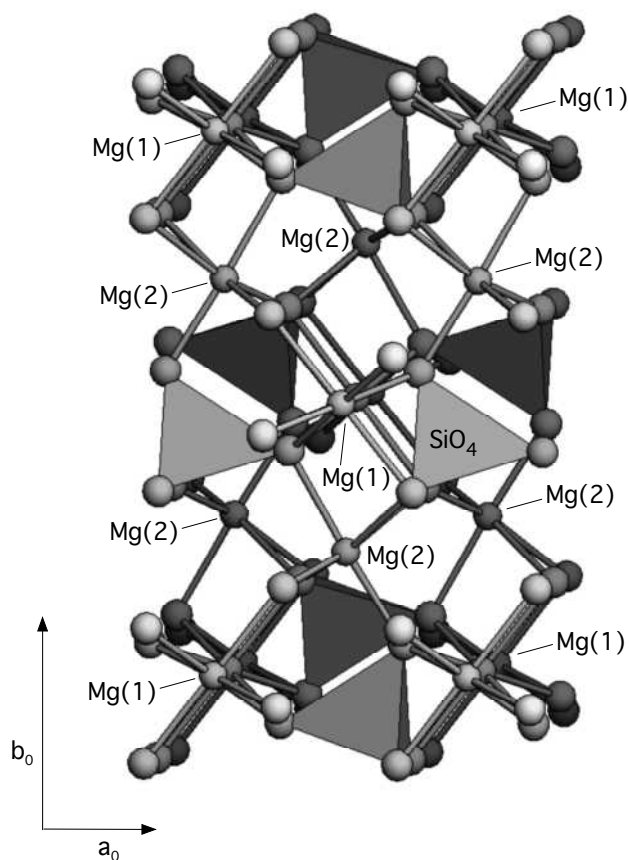


**FIGURE 1.** Forsterite structure (c axis projection) showing arrangements of the Mg1 and Mg2 octahedra. Mg-sites, SiO<sub>4</sub> tetrahedra, and axes are indicated.

progressively larger as mode frequencies increase to 1000 cm<sup>-1</sup>. Atomic displacements (eigenmodes) animations for forsterite as calculated by Noel et al. (2006) are displayed at [www.crystal.unito.it/vibs/forsterite/](http://www.crystal.unito.it/vibs/forsterite/). These results are in essential agreement with the experimental findings of Kolesov and Geiger (2004), who measured the effects of Mg isotope substitution on the powder Raman spectrum of forsterite.

The lattice dynamics study by Iishi (1978) achieved some success in fitting calculated fundamental mode frequencies to observed Raman frequencies by varying force constants for bond stretching (Mg-O and Si-O) and bond bending (O-Si-O). From these results, calculated modes and their associated eigenmodes could be assigned to specific Raman spectral features that are clearly separated in the observed spectra. In more structurally complex silicates, however, groups of overlapping modes within relatively narrow frequency ranges are commonly seen in the Raman spectra. See, for example, albite (NaAlSi<sub>3</sub>O<sub>8</sub>) (McKeown 2005). In these instances, it can be difficult to assign spectral features unambiguously to specific eigenmodes obtained from lattice dynamics calculations. Such ambiguities can often be reduced or even eliminated when calculated scattering intensities are available for comparison with experiment, as in the present work. The results can then also be used to develop models applicable to materials having mostly unknown structures, such as poorly crystalline and amorphous silicates.

## CRYSTAL STRUCTURE AND FACTOR GROUP ANALYSIS

The forsterite crystal structure is orthorhombic (Boström 1987), with space group symmetry *Pbnm* and four formula units in the unit cell. The crystal consists of isolated SiO<sub>4</sub> tetrahedra that are surrounded by MgO<sub>6</sub> octahedra occupying sites of two different symmetries (Fig. 1). The tetrahedra have three distinct Si-O distances ranging from 1.615 to 1.654 Å, while the two different Mg-octahedra have three distinct Mg1-O distances ranging from 2.070 to 2.131 Å and four distinct Mg2-O distances ranging from 2.047 to 2.213 Å. Factor group analysis (Noel et al. 2006; Kolesov and Geiger 2004; Chopelas 1991; Iishi 1978) indicates that forsterite has 84 vibrational modes, of which 36 are Raman-active (11 A<sub>g</sub> + 11 B<sub>1g</sub> + 7 B<sub>2g</sub> + 7 B<sub>3g</sub>). Due to site symmetry, the Raman-active modes have no Mg1 motion (inversion symmetry) but can have Mg2 motion (mirror plane symmetry).

## COMPUTATIONAL METHODOLOGY

As noted above, the present calculations are based on the local density approximation (LDA) of DFT and employ the ABINIT (Gonze et al. 2002, 2005b) software package. Troullier-Martins-type LDA pseudopotentials were used for Mg, Si, and oxygen (Troullier and Martins 1991). The phonon frequencies were obtained from a calculation of the dynamical matrix in the harmonic approximation. The Raman tensors were obtained analytically within DFPT as the third-order derivative of the energy with respect to two electric fields (incident and scattered photons) and one atomic displacement (phonon) (Veithen et al. 2005). This computational approach and this set of pseudopotentials were successfully used in previous calculations of Raman spectra on a variety of minerals, including MgSiO<sub>3</sub>, perovskite (Caracas and Cohen 2006) and ordered and disordered spinel (Caracas and Banigan 2009). As usual with planewave basis sets, the numerical accuracy of the calculation can be systematically improved by increasing the cut-off kinetic energy of the planewaves and the density of the sampling of the Brillouin zone (Payne et al. 1992). We used a 39 Ha (1 Ha = 27.21 eV) cut-off energy for the kinetic energy of the planewaves. We sampled the reciprocal space using a 4 × 2 × 4 regular grid of special k points according to the Monkhorst-Pack scheme (Monkhorst and Pack 1976). The computed lattice parameters are slightly underestimated (Tables 1a and 1b), as usual with LDA, with a maximum decrease of 1.9% along *b*. In previous first-principles calculations of the lattice dynamics of forsterite the relaxed unit-cell dimensions were slightly overestimated, where Noel et al. (2006) used the CRYSTAL code and a localized Gaussian-type basis set for the one-electron wavefunctions, while Meheut et al. (2009) used the generalized-gradient approximation to the exchange-correlation functional of Perdew et al. (1996). Other DFT calculations, summarized by Liu et al. (2009) have generally underestimated the cell dimensions.

## EXPERIMENTAL METHODS

The pure forsterite and fayalite samples measured in this study were Czochralski-grown single crystals that were used previously in thermal and optical studies by other investigators (Hofmeister 1987; Finch et al. 1980; Pertermann

**TABLE 1a.** Forsterite unit-cell parameters from experiment (Boström 1987) and after structural relaxation in the local density approximation of density functional theory

Unit-cell parameter	Experiment (Å)	Theory (Å)
<i>a</i>	4.755	4.685
<i>b</i>	10.199	10.002
<i>c</i>	5.979	5.873

**TABLE 1b.** Forsterite atomic fractional coordinates from experiment (Boström 1987) and after relaxation in the local density approximation of density functional theory

Atom	<i>x</i>		<i>y</i>		<i>z</i>	
	Expt.	Theory	Expt.	Theory	Expt.	Theory
Mg1	0	0	0	0	0	0
Mg2	0.9913	0.9913	0.2773	0.2762	0.25	0.25
Si	0.4261	0.4269	0.0940	0.0940	0.25	0.25
O1	0.7658	0.7684	0.0919	0.0916	0.25	0.25
O2	0.2210	0.2222	0.4470	0.4456	0.25	0.25
O3	0.2774	0.2754	0.1630	0.1636	0.0329	0.0313

**TABLE 2.** Forsterite  $A_g$  calculated Raman intensity and eigenmode comparisons

$\nu_{\text{obs}}$ ( $\text{cm}^{-1}$ )	$\nu_{\text{calc}}$ ( $\text{cm}^{-1}$ )	Calculated Raman intensity ( $\times 10^{11}$ atomic units)	ABINIT	Iishi (1)	Chopelas (2)	K&G (3)
966	962	(xx) = 204 000 (yy) = 213 000 (zz) = 286 000	Si-O stretch; $\text{SiO}_4$ breathing $\nu_3$	$\nu_3$	$\nu_3$	$\nu_3$
856	849	(xx) = 702 100 (yy) = 193 000 (zz) = 841 000	Si-O stretch; $\text{SiO}_4$ breathing $\nu_3$	$\nu_3$	$\nu_1 + \nu_3$	$\nu_1 + \nu_3$
826	819	(xx) = 1 190 000 (yy) = 1 140 000 (zz) = 506 000	Si-O stretch, $\nu_3$	$\nu_1$	$\nu_1 + \nu_3$	$\nu_1 + \nu_3$
609	606	(xx) = 164 000 (yy) = 26 700 (zz) = 41 500	$\nu_4$	$\nu_4$	$\nu_4$	$\nu_4$
546	540	(xx) = 4080 (yy) = 29 300 (zz) = 1140	$\text{Si} \pm y, \nu_4$	$\nu_4$	$\nu_4$	$\nu_4$
423	436	(xx) = 4750 (yy) = 12 000 (zz) = 27 700	$\text{Mg}2 \pm xy; \text{SiO}_4 \pm xy, \nu_2$	$\nu_2$	$\nu_2$	$\nu_2$
340	357	(xx) = 474 (yy) = 20 100 (zz) = 14 100	$\text{Mg}2 \pm xy; \text{SiO}_4$ rot. $\parallel z$	$\text{SiO}_4$ rot. $\parallel z$	M2 trans.	$\text{R}(\text{SiO}_4) + \text{M}2$
329	337	(xx) = 6300 (yy) = 12 600 (zz) = 10 900	$\text{Mg}2 \pm y; \text{SiO}_4$ rot. $\parallel z$	$\text{Mg}2 \pm y$	$\text{SiO}_4$ rot.	$\text{R}(\text{SiO}_4) + \text{M}2$
305	318	(xx) = 16 400 (yy) = 1230 (zz) = 10 600	$\text{Mg}2 \pm xy; \text{SiO}_4 \pm xy$ rot. $\parallel z$	$\text{Mg}2, \text{SiO}_4 \pm x$	M2 trans.	$\text{R}(\text{SiO}_4) + \text{M}2$
227	227	(xx) = 5640 (yy) = 6890 (zz) = 3090	$\text{Mg}2, \text{SiO}_4 \pm y$	$\text{Mg}2, \text{SiO}_4 \pm y$	$\text{SiO}_4$ trans.	$\text{T}(\text{SiO}_4) + \text{M}2$
183	190	(xx) = 975 (yy) = 790 (zz) = 177	$\text{Mg}2 \pm x, \text{SiO}_4 \pm x$ (shear), minor $\nu_3$	$\text{Mg}2, \text{SiO}_4 \pm x$	$\text{SiO}_4$ trans.	$\text{T}(\text{SiO}_4) + \text{M}2$

Notes: Average  $|\nu_{\text{obs}} - \nu_{\text{calc}}| = 7.7 \text{ cm}^{-1}$ . (1) = Iishi 1978; (2) = Chopelas 1991; (3) = Kolesov and Geiger 2004.

and Hofmeister 2006). Both crystals were roughly plate-shaped and less than 0.5 cm in diameter. The forsterite crystal was clear and colorless, while the fayalite sample was a dark green, opaque crystal. Each crystal was mounted on a spindle stage so that the crystallographic axes of the sample could be precisely oriented with respect to the directions of propagation and polarization of the incident and scattered light.

Raman spectra were collected using a single-grating spectrograph and notch filter system (Goncharov and Struzhkin 2003). A Melles-Griot Model 45 Ar<sup>+</sup> laser provided the 5145 Å wavelength incident light that was directed through a broad band polarization rotator (Newport Model PR-550) to the microscope that guided the laser light down to the sample surface through a Mitutoyo 10× microscope objective (38 mm working distance, 0.23 numerical aperture). Approximately 17 mW of laser power was focused to a 10 μm diameter spot on each sample fragment. Parallel-polarized ( $A_g$ ) and cross-polarized ( $B_{1g}$ ,  $B_{2g}$ , and  $B_{3g}$ ) spectra were obtained by rotating the incident polarization before it entered the microscope. The scattered light from the sample was directed through a polarization analyzer in the microscope column, which was maintained in a fixed orientation for all polarized spectra collected. After the analyzer, the scattered light proceeded through holographic notch and super-notch filters (Kaiser Optical Systems), which reduced the Rayleigh scattered light intensity by as much as ten orders of magnitude. The notch filters were oriented in the scattered light path to provide adequate rejection of the Rayleigh scattering to within 70  $\text{cm}^{-1}$  of the excitation line. The spectrograph (JY-Horiba HR460) used an 1800 gr/mm grating (Richardson Grating Laboratory) to disperse the Stokes scattered light from the sample on to a 2048 × 512 element Peltier-cooled CCD detector (Andor Technology Model DU440BV). The spectrograph was frequency calibrated using a Ne lamp and Raman scattering from  $\text{CCl}_4$ , so that the recorded frequencies are accurate to within  $\pm 1 \text{ cm}^{-1}$  of actual values. The entrance slits of the JY-Horiba HR460 spectrograph were set to provide 2  $\text{cm}^{-1}$  resolution in the measured spectra. Each  $A_g$  spectrum is an average of forty 10 s accumulations, while each  $B_g$  spectrum is an average of eighty 10 s accumulations.

The Raman spectra were then corrected for the effects of the notch filter on the scattered light intensity, as well as for grating and detector quantum efficiencies over the frequency range measured. Each corrected spectrum was then processed to produce a reduced Raman spectrum (Born and Huang 1954) (Figs. 2 and 3) by dividing the Raman intensity by the Bose-Einstein distribution and by  $\omega_i^3$ , where  $\omega_i$

is the frequency of the Raman-scattered radiation. This calibration permits direct, quantitative comparison of spectral intensities obtained in different scattering geometries and allows all measurements to be compared to theoretical predictions using a single scaling parameter.

## RESULTS AND DISCUSSION

The  $A_g$  and B modes obtained for forsterite (Figs. 2 and 3) are similar to those presented by previous studies (Chopelas 1991; Iishi 1978). The Raman-scattering amplitudes of even the most intense high-frequency features in the  $B_{1g}$ ,  $B_{2g}$ , and  $B_{3g}$  spectra (Fig. 3) are at least an order of magnitude weaker than those in the  $A_g$  spectra (Fig. 2), making it difficult to avoid contamination of the B-symmetry spectra. The forsterite crystal was oriented with respect to the incident laser light so as to minimize leakage, but the microscope objective produces a relatively large solid angle of illumination and collection at the sample, making it impossible to avoid some contamination of each of the B-symmetry spectra, especially at higher frequencies, by the stronger  $A_g$  modes and one or two of the other B-species modes (Fig. 3).

The calculated fundamental mode frequencies and intensities for the six different scattering geometries are in reasonable agreement with the six characteristic Raman spectra (Tables 2–5; Figs. 2 and 3). Calculated frequencies for modes above 500  $\text{cm}^{-1}$  are higher than observed by 4 to 7  $\text{cm}^{-1}$ , while calculated values for modes below 500  $\text{cm}^{-1}$  are 0 to 17  $\text{cm}^{-1}$  lower than observed. The Raman susceptibility output by ABINIT for each calculated mode was squared to produce the calculated Raman intensity. The calculated Raman intensity at the calculated frequency for each mode was then plotted with the corresponding Raman

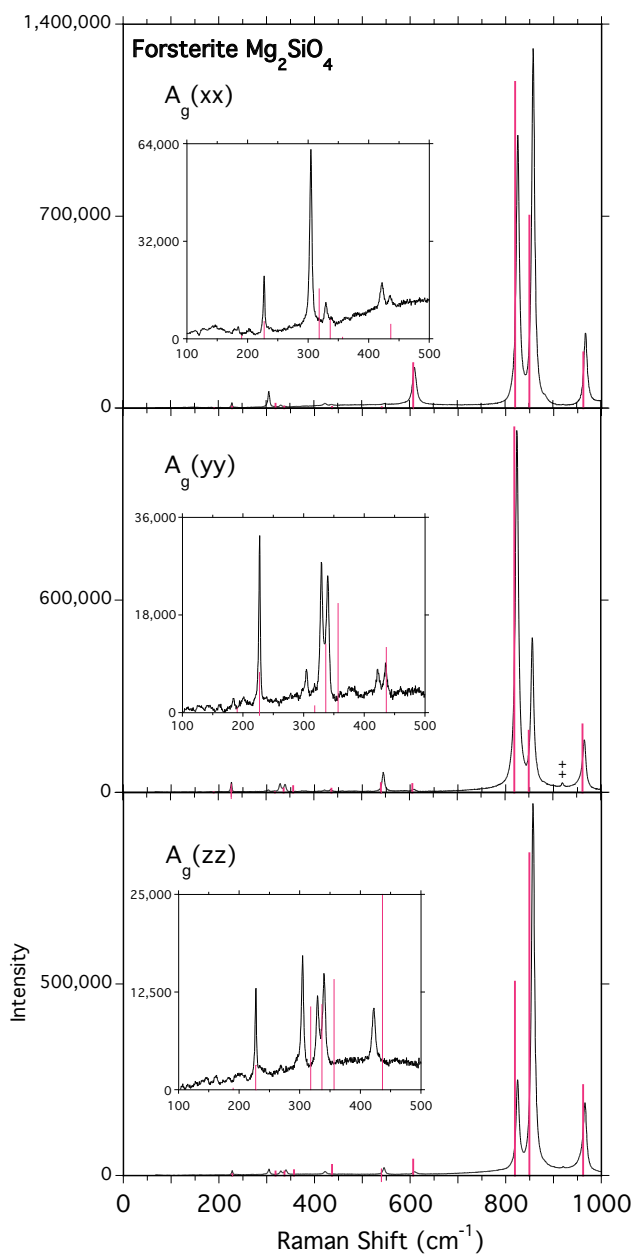


**FIGURE 2.** The three characteristic reduced  $A_g$  spectra for forsterite, where the inset for each geometry shows details of the relatively weak Raman modes below  $500\text{ cm}^{-1}$ . Calculated modes are plotted as red bars, where intensity values are in  $10^{11}$  atomic units. The reduced experimental spectra are scaled by  $5 \times 10^{16}$  so that the  $826\text{ cm}^{-1}$   $A_g(yy)$  peak intensity agrees with the intensity of the calculated  $819\text{ cm}^{-1}$  mode. ‡ Indicates leakage from a  $B_{3g}$  species mode. Note color online.

spectrum (Figs. 2 and 3). The intensities of all measured spectra were rescaled by  $5 \times 10^{16}$ . This rescaling matches the amplitude of the  $826\text{ cm}^{-1}$  peak in the reduced  $A_g(yy)$  spectrum (Fig. 2 middle) with the theoretical intensity of the corresponding  $819\text{ cm}^{-1}$   $A_g(yy)$  calculated mode. Calculated Raman intensity values span a range of up to six orders of magnitude (Tables 2 to 5) and agree quite well with the observed spectra (Figs. 2 and 3). Two of the largest amplitude discrepancies are found for the  $866\text{ cm}^{-1}$   $B_{1g}$  and  $882\text{ cm}^{-1}$   $B_{2g}$  modes, where the calculated intensities

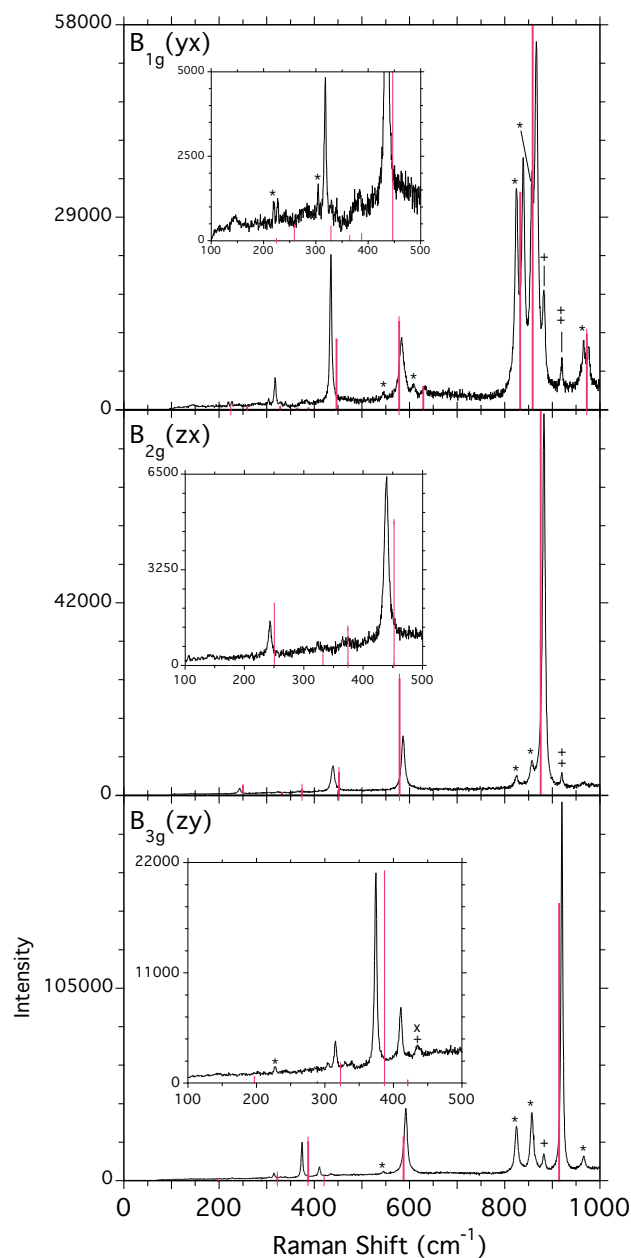


**FIGURE 3.** The three characteristic reduced  $B_{1g}$ ,  $B_{2g}$ , and  $B_{3g}$  spectra for forsterite. Conventions in Figure 2 are followed. Leakage from an  $A_g$ ,  $B_{1g}$ ,  $B_{2g}$ , or  $B_{3g}$  mode is indicated by the symbol \*, x, +, or ‡, respectively. Note color online.

are both approximately 2.5 times larger than observed (plotted off-scale in Figs. 3 top and middle).

Our results (Tables 2–5) indicate that, in general, Raman-active phonons below  $500\text{ cm}^{-1}$  are lattice modes, where the  $\text{SiO}_4$  tetrahedra act as rigid units and Mg2 translations are mixed with  $\text{SiO}_4$  rotations and translations. The Raman modes above  $500\text{ cm}^{-1}$  have atomic displacements dominated by motions internal to the  $\text{SiO}_4$  tetrahedra. These internal modes are conveniently described using the conventional tetrahedral mode labels  $\nu_1$

**TABLE 3.** Forsterite B<sub>1g</sub> calculated Raman intensity and eigenmode comparisons

$\nu_{\text{obs}}$ (cm <sup>-1</sup> )	$\nu_{\text{calc}}$ (cm <sup>-1</sup> )	Calculated Raman intensity ( $\times 10^{11}$ atomic units)	ABINIT	lishi (1)	Chopelas (2)	K&G (3)
976	972	11 300	Si $\pm$ x $\nu_3$	$\nu_3$	$\nu_3$	
866	859	135 000	$\nu_{3c}$ Si $\pm$ y	$\nu_3$	$\nu_3$ (+ $\nu_1$ )	$\nu_3$ (+ $\nu_1$ )
839	832	32 700	$\nu_1$ Si $\pm$ y	$\nu_1$	$\nu_1$ (+ $\nu_3$ )	$\nu_1$ (+ $\nu_3$ )
632	629	3450	Si $\pm$ x $\nu_4$ ; Mg2 $\pm$ y.	$\nu_4$	$\nu_4$	
583	578	13 200	Mg2 $\pm$ y; SiO <sub>4</sub> ; $\nu_4$ Si $\pm$ x	$\nu_4$	$\nu_4$	$\nu_4$
434	447	10 600	Mg2 $\pm$ x; $\nu_2$	$\nu_2$	$\nu_2$	$\nu_2$
384	387	214	Mg2 $\pm$ y; $\nu_4$ Si $\pm$ y	SiO <sub>4</sub> rot.    z	M2 trans.	
374?	365	3030	SiO <sub>4</sub> rot.    z	??	M2 trans.	
318	329	428	Mg2 $\pm$ xy; SiO <sub>4</sub> $\pm$ x def.( $\nu_{4b}$ )	Mg2 $\pm$ y	SiO <sub>4</sub> rot.	R(SiO <sub>4</sub> ) + M2
275(?)*	259	471	Mg2 $\pm$ xy; SiO <sub>4</sub> $\pm$ xy def.( $\nu_{4b}$ )	Mg2, SiO <sub>4</sub> $\pm$ x	SiO <sub>4</sub> trans.	
227	225	1	Mg2 $\pm$ x; SiO <sub>4</sub> $\pm$ y	Mg2, SiO <sub>4</sub> $\pm$ x	SiO <sub>4</sub> trans.	

Notes: Average  $|\nu_{\text{obs}} - \nu_{\text{calc}}| = 7.0$  cm<sup>-1</sup>. (1) = lishi 1978; (2) = Chopelas 1991; (3) = Kolesov and Geiger 2004.

\* lishi (1978) observed a 260 cm<sup>-1</sup> mode; Chopelas (1991) observed a 274 cm<sup>-1</sup> mode.

**TABLE 4.** Forsterite B<sub>2g</sub> calculated Raman intensity and eigenmode comparisons

$\nu_{\text{obs}}$ (cm <sup>-1</sup> )	$\nu_{\text{calc}}$ (cm <sup>-1</sup> )	Calculated Raman intensity ( $\times 10^{11}$ atomic units)	ABINIT	lishi (1)	Chopelas (2)	K&G (3)
882	875	207 000	$\nu_3$	$\nu_3$	$\nu_3$	$\nu_3$
588	580	25 300	$\nu_4$	$\nu_4$	$\nu_4$	$\nu_4$
441	452	4880	Mg2 $\pm$ z; SiO <sub>4</sub> def. $\nu_2$	$\nu_2$	$\nu_2$	$\nu_2$
368	374	1270	SiO <sub>4</sub> rot.    y shear yz	SiO <sub>4</sub> rot.    y	Mix SiO <sub>4</sub> rot.	
324	332	395	Mg2 $\pm$ z; SiO <sub>4</sub> $\pm$ z (shear)	SiO <sub>4</sub> rot.    x	Mix M2 trans.	
244	250	2120	SiO <sub>4</sub> rot.    x; Mg2 $\pm$ z	SiO <sub>4</sub> $\pm$ z	Mix SiO <sub>4</sub> rot.	T(SiO <sub>4</sub> ) + M2
? (175*)	178	3	Mg2 $\pm$ z; SiO <sub>4</sub> rot.    x	Mg2 $\pm$ z	Mix SiO <sub>4</sub> trans.	

Notes: Average  $|\nu_{\text{obs}} - \nu_{\text{calc}}| = 7.0$  cm<sup>-1</sup>. (1) = lishi 1978; (2) = Chopelas 1991; (3) = Kolesov and Geiger 2004.

\* Observed by Chopelas (1991).

**TABLE 5.** Forsterite B<sub>3g</sub> calculated Raman intensity and eigenmode comparisons

$\nu_{\text{obs}}$ (cm <sup>-1</sup> )	$\nu_{\text{calc}}$ (cm <sup>-1</sup> )	Calculated Raman intensity ( $\times 10^{11}$ atomic units)	ABINIT	lishi (1)	Chopelas (2)	K&G (3)
922	914	151 000	$\nu_3$	$\nu_3$	$\nu_3$	$\nu_3$
595	587	23 600	$\nu_4$ ; Mg2 $\pm$ z	$\nu_4$	$\nu_4$	$\nu_4$
411	421	33	$\nu_2$	$\nu_2$	$\nu_2$	$\nu_2$
376	387	20 900	Mg2 $\pm$ y; SiO <sub>4</sub> rot.    x (and y).	SiO <sub>4</sub> rot.    z	Mix M2 trans.	R(SiO <sub>4</sub> ) + M2
318	323	1750	Mg2 $\pm$ z; SiO <sub>4</sub> rot.    y	SiO <sub>4</sub> rot.    y	Mix (SiO <sub>4</sub> rot.)	R(SiO <sub>4</sub> ) + M2
272	289	182	SiO <sub>4</sub> $\pm$ z rot.    x; Mg2 $\pm$ z	Mg2 $\pm$ z	Mix (SiO <sub>4</sub> trans.)	
203?*	197	606	Mg2 $\pm$ z; SiO <sub>4</sub> rot.    x	SiO <sub>4</sub> rot.    z		

Notes: Average  $|\nu_{\text{obs}} - \nu_{\text{calc}}| = 9.3$  cm<sup>-1</sup>. (1) = lishi 1978; (2) = Chopelas 1991; (3) = Kolesov and Geiger 2004. Chopelas (1991) lists 435 cm<sup>-1</sup> B<sub>3g</sub>; this mode is observed in our B<sub>3g</sub> spectrum, but as leakage from B<sub>1g</sub>.

\* lishi (1978) lists 206 cm<sup>-1</sup>.

through  $\nu_4$ , as illustrated in Lam et al. (1990). The eigenmodes calculated in this study are nearly identical with those obtained by Noel et al. (2006), and are in qualitative agreement with other forsterite studies (Kolesov and Geiger 2004; Chopelas 1991; lishi 1978).

In many cases, the relative intensities of Raman-active modes in forsterite can be correlated with the type of atomic displacements involved (Tables 2–5), when both site symmetry and atomic polarizability are taken into account. In a crystal with inversion symmetry, the motion of atoms located at centrosymmetric sites cannot contribute to the scattering intensity. As the site symmetry of an atom deviates more from inversion symmetry, we expect the Raman intensity of modes involving motion of that atom to increase. In forsterite, the Mg1 atoms occupy centrosymmetric sites and cannot contribute to Raman scattering. The other species occupy sites with increasing deviations from inversion symmetry, in the order Mg2, Si, and O. Modes at higher frequencies, especially above 800 cm<sup>-1</sup>, are the most intense and have atomic motions internal to the SiO<sub>4</sub> tetrahedra. These internal tetrahedral modes are dominated by displacements within the highly polarizable oxygen environments surrounded by covalently bonded Si and ionically bonded Mg<sup>2+</sup>, which probably amplify Raman intensity. Below 500 cm<sup>-1</sup>, lattice modes are dominated by displacements within the less polarizable Mg2 environments and are relatively weak. The above observations

are consistent with the expectation that the strongest intensity Raman modes involve the SiO<sub>4</sub> tetrahedra, while weaker modes involve Mg2O<sub>6</sub> groups, and the weakest (or inactive) modes involve the Mg1 octahedra.

Differences between calculated and observed frequencies for each mode also generally correlate with the type of atomic displacements for that mode. Most internal SiO<sub>4</sub> modes have calculated frequencies lower than the corresponding observed frequencies, while Mg2-related or lattice modes have calculated frequencies higher than the corresponding observed frequencies. These correlations may indicate that the planewave basis used in the present calculation produces errors in the Raman tensor of opposite sign for relatively localized and delocalized states. The calculation of Noel et al. (2006), which uses a basis of localized (Gaussian) wavefunctions, does not show this pattern.

The Fe end-member of the olivine solid-solution series, fayalite (Fe<sub>2</sub>SiO<sub>4</sub>), exhibits non-collinear magnetism and its accurate treatment within DFT requires a more advanced formalism, such as DFT+U (Cococcioni et al. 2003; Jiang et al. 2004). In principle, this formalism could be used in a frozen-phonon calculation of the vibrational frequencies. Computing the Raman tensor in ABINIT using the DFT+U formalism is not yet possible, however, so we only present the experimental results for fayalite (Fig. 4) for comparison with the forsterite results (Figs. 2–3). The fayalite structure (Kadon and Takeda 1986) has the same features,

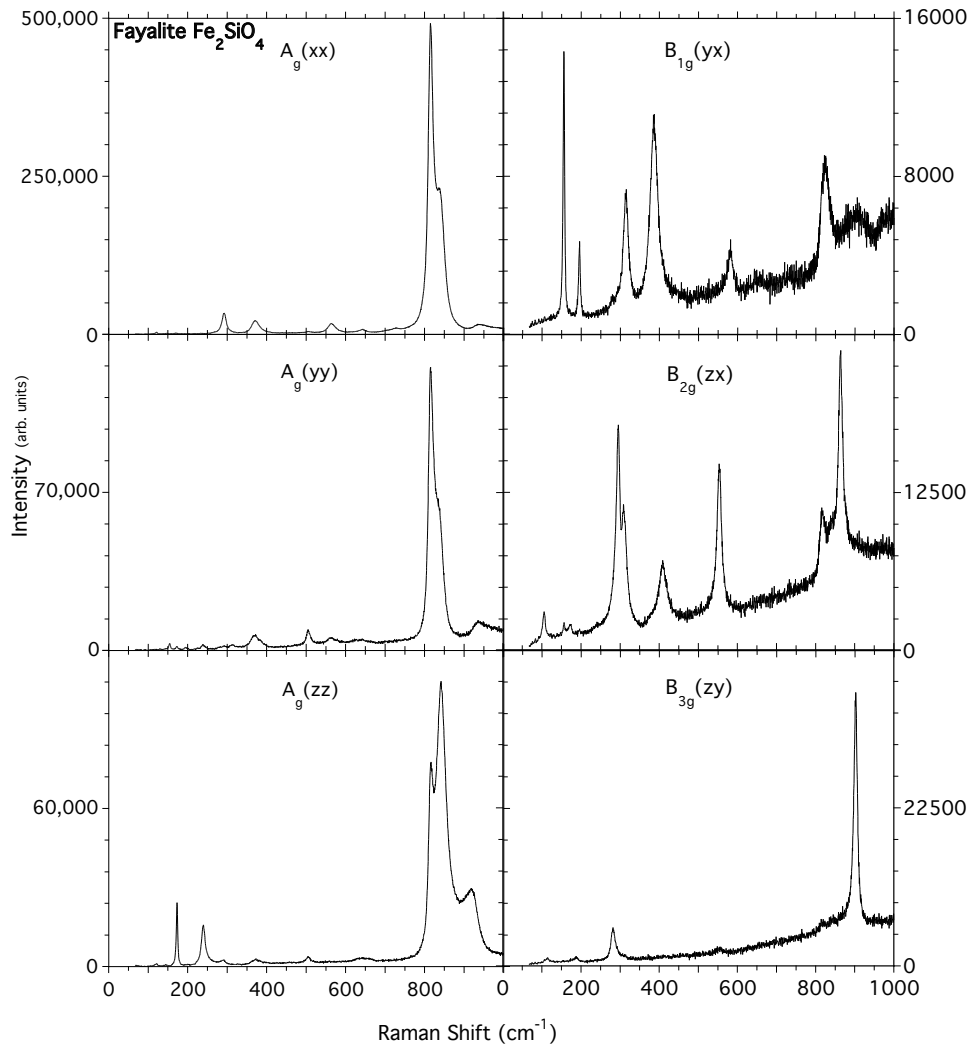


FIGURE 4. The six characteristic reduced spectra for fayalite, As in Figure 2, the reduced spectra are scaled by  $5 \times 10^{16}$ .

symmetry, and factor group analysis results as those outlined above for forsterite, except that Fe substitutes for Mg.

The six fayalite spectra (Fig. 4) are similar to those reported previously (Chopelas 1991) but with improved signal-to-noise in some of the B-species data. At frequencies greater than  $500 \text{ cm}^{-1}$ , fayalite exhibits spectral features similar to those of forsterite, except that peaks are generally broadened and shifted to lower frequencies by approximately 5 to  $45 \text{ cm}^{-1}$ , as seen earlier (Chopelas 1991). This trend can be understood by noting that the modes in question involve coupling of internal  $\text{SiO}_4$  tetrahedral vibrations to the neighboring octahedral metal cations. The crystal with the heavier metal cations, in this case fayalite with Fe, would be expected to have the lower frequency modes. Below  $500 \text{ cm}^{-1}$ , the trends are not as obvious. Here, Fe displacements probably mix with  $\text{SiO}_4$  rotations and translations, and the magnetic characteristics of Fe may have more significant influence on Raman peak frequencies and relative intensities. Once it becomes possible to calculate Raman modes for fayalite, we should be able to verify these explanations on the basis of first-principles theory.

#### ACKNOWLEDGMENTS

We thank Anne Hofmeister (Department of Earth and Planetary Sciences, Washington University, St. Louis) for providing the forsterite and fayalite samples used in this study. We also appreciate conversations with Ronald Cohen (Geophysical Laboratory, Carnegie Institution) regarding the ABINIT package and the application of density functional theory. Calculations were performed on one of the high performance parallel computing platforms at the Centre Informatique National de l'Enseignement Supérieur (Montpellier, France) under grant st12816.

#### REFERENCES CITED

- Baroni, S., de Gironcoli, S., Dal Corso, A., and Giannozzi, P. (2001) Phonons and related crystal properties from density-functional perturbation theory. *Reviews in Modern Physics*, 73, 515–562.
- Born, M. and Huang, H. (1954) *Dynamical Theory of Crystal Lattices*, p. 199. Clarendon Press, Oxford.
- Boström, D. (1987) Single-crystal X-ray diffraction studies of synthetic Ni-Mg olivine solid solutions. *American Mineralogist*, 72, 965–972.
- Caracas, R. and Banigan, E. (2009) Elasticity and Raman spectra of  $\text{MgAl}_2\text{O}_4$  spinel from density functional perturbation theory. *Physics of the Earth and Planetary Interiors*, 174, 113–121.
- Caracas, R. and Cohen, R.E. (2006) Theoretical determination of the Raman spectra of  $\text{MgSiO}_3$  perovskite and post-perovskite at high pressure. *Geophysical Research Letters*, 33, L12S05, DOI: 10.1029/2006GL025736.
- Chopelas, A. (1991) Single crystal Raman spectra of forsterite, fayalite, and monticellite. *American Mineralogist*, 76, 1101–1109.
- Cococcioni, M., Dal Corso, A., and de Gironcoli, S. (2003) Structural, electronic,

- and magnetic properties of  $\text{Fe}_2\text{SiO}_4$  fayalite: Comparison of LDA and GGA results. *Physical Review B*, 67, 094106.
- Finch, C.B., Clark, G.W., and Koop, O.C. (1980) Czochralski growth of single-crystal fayalite under controlled oxygen fugacity conditions. *American Mineralogist*, 65, 381–389.
- Goncharov, A.F. and Struzhkin, V.V. (2003) Raman spectroscopy of metals, high-temperature superconductors and related materials under high pressure. *Journal of Raman Spectroscopy*, 34, 532–548.
- Gonze, X., Beuken, J.M., Caracas, R., Detraux, F., Fuchs, M., Rignanese, G.-M., Sindic, L., Verstraete, M., Zerah, G., Jollet, F., Torrent, M., Roy, A., Mikami, M., Ghosez, P., Raty, J.Y., and Allan, D.C. (2002) First-principle computation of material properties: the ABINIT software project. *Computational Materials Science*, 25, 478–492.
- Gonze, X., Rignanese, G.-M., and Caracas, R. (2005a) First-principle studies of the lattice dynamics of crystals, and related properties. *Zeitschrift für Kristallographie*, 220, 458–472.
- Gonze, X., Rignanese, G.-M., Verstraete, M., Beuken, J.-M., Pouillon, Y., Caracas, R., Jollet, F., Torrent, M., Zerah, G., Mikami, M., Ghosez, P., Veithen, M., Olevano, V., Reining, L., Godby, R., Onida, G., Hamann, D., and Allan, D.C. (2005b) A brief introduction to the ABINIT software package. *Zeitschrift für Kristallographie*, 220, 558–562.
- Hofmeister, A.M. (1987) Single-crystal absorption and reflection infrared spectroscopy of forsterite and fayalite. *Physics and Chemistry of Minerals*, 14, 499–513.
- Iishi, K. (1978) Lattice dynamics of forsterite. *American Mineralogist*, 63, 1198–1208.
- Jiang, X. and Guo, G.Y. (2004) Electronic structure, magnetism, and optical properties of  $\text{Fe}_2\text{SiO}_4$  fayalite at ambient and high pressures: A GGA+ $U$  study. *Physical Review B*, 69, 155108.
- Kohn, W. and Sham, L.J. (1965) Self-consistent equations including exchange and correlation effects. *Physical Review*, 140, A1133–A1138.
- Kolesov, B.A. and Geiger, C.A. (2004) A Raman spectroscopic study of Fe-Mg olivines. *Physics and Chemistry of Minerals*, 31, 142–154.
- Kudoh, Y. and Takeda, H. (1986) Single crystal X-ray diffraction study on the bond compressibility of fayalite,  $\text{Fe}_2\text{SiO}_4$  and rutile,  $\text{TiO}_2$  under high pressure. *Physica B+C*, 139–140, 333–336.
- Lam, P.K., Yu, R., Lee, M.W., and Sharma, S.K. (1990) Structural distortions and vibrational modes in  $\text{Mg}_2\text{SiO}_4$ . *American Mineralogist*, 75, 109–119.
- Liu, L., Du, J., Zhao, J., Liu, H., Gao, H., and Chen, Y. (2009) Elastic properties of hydrous forsterites under high pressure: First-principle calculations. *Physics of the Earth and Planetary Interiors*, 176, 89–97.
- McKeown, D.A. (2005) Raman spectroscopy and vibrational analyses of albite: From 25 °C through the melting temperature. *American Mineralogist*, 90, 1506–1517.
- Meheut, M., Lazzeri, M., Balan, E., and Mauri, F. (2009) Structural control over equilibrium silicon and oxygen isotopic fractionation: A first-principles density-functional theory study. *Chemical Geology*, 258, 28–37.
- Monkhorst, H.J. and Pack, J.D. (1976) Special points for Brillouin-zone integrations. *Physical Review B*, 13, 5188–5192.
- Mouri, T. and Enami, M. (2008) Raman spectroscopic study of olivine-group materials. *Journal of Mineralogical and Petrological Sciences*, 103, 100–104.
- Noel, Y., Catti, E.M., D'Arco, Ph., and Dovesi, R. (2006) The vibrational frequencies of forsterite  $\text{Mg}_2\text{SiO}_4$ : An all-electron ab initio study with the CRYSTAL code. *Physics and Chemistry of Minerals*, 33, 383–393.
- Payne, M.C., Teter, M.P., Allan, D.C., Arias, T.A., and Joannopoulos, J.D. (1992) Iterative minimization techniques for *ab initio* total-energy calculations: Molecular dynamics and conjugate gradients. *Reviews in Modern Physics*, 64, 1045–1097.
- Perdew, J.P., Burke, K., and Ernzerhof, M. (1996) Generalized gradient approximation made simple. *Physical Review Letters*, 77, 3865–3868.
- Pertermann, M. and Hofmeister, A.M. (2006) Thermal diffusivity of olivine-group minerals at high temperature. *American Mineralogist*, 91, 1747–1760.
- Troullier, N. and Martins, J.L. (1991) Efficient pseudopotentials for plane-wave calculations. *Physical Review B*, 43, 1993–2006.
- Veithen, M., Gonze, X., and Ghosez, P. (2005) Nonlinear optical susceptibilities, Raman efficiencies, and electro-optic tensors from first-principles density functional perturbation theory. *Physical Review B*, 71, 125107.

MANUSCRIPT RECEIVED OCTOBER 14, 2009  
 MANUSCRIPT ACCEPTED FEBRUARY 2, 2010  
 MANUSCRIPT HANDLED BY ARTEM OGANOV